Metal anomalies in zircon as a record of granite-hosted mineralization

Nicholas J. Gardiner[1,2*], Chris J. Hawkesworth[1,3], Laurence J. Robb[4,5,6], Jacob A. Mulder[2], Ashlea N. Wainwright[2,7], Peter A. Cawood[1,2]

[1]School of Earth and Environmental Sciences, University of St. Andrews, St. Andrews KT16 9AL, UK.

[2]School of Earth, Atmosphere and Environment, Monash University, Victoria 3800, Australia.

[3]School of Earth Sciences, University of Bristol, Bristol BS8 1RJ, UK.

[4]Department of Earth Sciences, University of Oxford, South Parks Road, Oxford OX1 3AN, UK.

[5]School of Geosciences, University of the Witwatersrand, Johannesburg, South Africa.

[6]DSI-NRF CIMERA, University of Johannesburg, South Africa.

[7]School of Earth Sciences, University of Melbourne, Victoria 3010, Australia.

*nick.gardiner@st-andrews.ac.uk

ABSTRACT

Granite-hosted magmatic-hydrothermal mineral deposits are major sources of Cu, Mo, Sn, Li, and W, originating via mineralizing fluids exsolved from volatile-saturated magmas. We show how trace elements in zircon sampled from the granite-hosted Zaaiplaats tin deposit, Bushveld Complex, preserve a record of both the enrichment of incompatible metals during magma fractionation and those arising from magmatic-hydrothermal mineralization processes. The Zaaiplaats granites are subdivided into three groups; mineralized, altered, and unmineralized. Zircon trace element contents define two trends in a plot of Sn against Gd: Sn/Gd ratios in zircons from the unmineralized samples, as well as the majority of altered samples, define a magma fractionation trend with increasing Y at constant Sn/Gd, whereas those from the mineralized samples are displaced to high Sn/Gd ratios at similar Y. Elevated Sn in the Zaaiplaats zircons is attributed to the introduction of a Sn-rich mineralizing fluid during zircon growth, which occurred at an advanced stage of crystallization (>85 %) of the host magma. This model is consistent with the preservation of whole-rock Sn zonation in the Zaaiplaats granites modelled by closed-system magma differentiation and the ensuing exsolution of an acidic, saline Sn-rich magmatic-hydrothermal fluid (Groves and McCarthy, 1978). A metal anomaly, Sn/Sn*, is defined which describes the deviation of Sn over that expected through magma fractionation alone (Sn*), and arises from Sn mobilization due to magmatic-hydrothermal mineralization processes. Identification of metal anomalies such as Sn/Sn* and Cu/Cu* in mineral archives or at the whole-rock level, provides an empirical link to the onset of mineralization processes in magmatic-hydrothermal systems, and can be coupled with geochemical proxies to yield a better understanding of the conditions leading up to, and subsequent to, volatile saturation.

1. Introduction

Granite-associated magmatic-hydrothermal mineral deposits, whether intrusion, vein, or pegmatite related, are major economic sources of Cu, Mo, Au, Sn, Li, and W. These deposits originate from intermediate to felsic magmas emplaced within the mid- to upper-continental crust (Burnham, 1997; Černý et al., 2005; Sillitoe, 2010). Volatiles, together with fluid-mobile elements, initially dissolved in the magma, exsolve during the process of aqueous/volatile saturation, or degassing (Hedenquist and Lowenstein, 1994; Keppler and Wyllie, 1991; Sillitoe, 2010). Volatile exsolution, and the associated extraction of metals from magmas into these hydrothermal fluids, is a precursor to the ultimate precipitation of ore minerals, and represents a critical step in the genesis of magmatic-hydrothermal deposits (Candela, 1997; Heinrich, 1990; Wilkinson, 2013). A key requirement is the reliable identification in natural mineral archives of criteria heralding the onset of fluid-related mineralization versus that of magma fractionation.

Experimental and empirical studies of volatile saturation primarily in Cu porphyry systems, have sought to relate the role of volatile saturation to the relative contributions of magma fertility, volatile phase solubilities, and the volume and rates of magma injection (e.g., Audetat et al., 1998; Blundy et al., 2015; Chelle-Michou et al., 2017; Heinrich et al., 1999; Williams-Jones and Heinrich, 2005). Recent experimental work on Sn-W deposits has however challenged the paradigm that Sn strongly partitions into the vapour phase during volatile saturation, instead remaining concentrated within the magma under some circumstances (Duc-Tin et al., 2007; Schmidt et al., 2020).

The genesis and evolution of magmas govern their ability to generate metal-rich fluids that ultimately form ore deposits (Blevin and Chappell, 1992; Černý et al., 2005; Hart et al., 2004; Williams-Jones and Heinrich, 2005). Advances in our understanding of such petrogenetic processes have been achieved through *in-situ* geochemical analytical techniques, principally applied to the silicate mineral zircon (Hoskin, 2003;

Kemp and Hawkesworth, 2013). Zircon is a robust accessory mineral common in evolved rocks, and its chemistry is sensitive to the conditions and processes that promote mineralization, including redox and fractionation (e.g., Ballard et al., 2002; Dilles et al., 2015; Gardiner et al., 2017). Thus, zircon has considerable potential to record the timing, and the conditions, associated with mineralization in magmatic systems.

Previous studies have looked at the use of zircon chemistry as a pathfinder to granite-hosted mineralization, such as the role of zircon rare earth elements (REE) to assess Cu porphyry prospectivity (Ballard et al., 2002; Dilles et al., 2015; Lu et al., 2016), linking trace element concentrations with U–Pb ages to decipher stages of metal enrichment, and interaction of zircon with hydrothermal fluids in polymetallic magmatic-hydrothermal systems (Jiang et al., 2020; Li et al., 2014).

In this contribution we explore how zircon trace element contents, including those of metals of economic interest, trace the effects of magma-fluid evolution associated with granite-hosted mineralization by examining samples from a mineralized portion of the Lebowa Granite Suite, at the polymetallic Zaaiplaats Tin Mine, Bushveld Complex, South Africa. We focus on how zircon mineral chemistry in an evolving granite system records and discriminates between the processes of magmatic fractionation and that of metal enrichment associated with co-genetic magmatic-hydrothermal fluids. In doing so, we define metal anomalies that fingerprint the onset of mineralization processes, which in the case of Zaaiplaats the anomaly Sn/Sn* provides a parameter linking empirical indicators of magmatic processes with the onset of tin mineralization.

2. The Zaaiplaats Sn Deposit

The A-type Lebowa Granite Suite (LGS) of the Bushveld Complex, contains polymetallic (Sn-W-Mo-Cu-Pb-Zn-F) styles of mineralization (Robb et al., 2000). These

98 granites, emplaced as large sills at ca. 2.054 Ga (Walraven and Hattingh, 1993),
99 overlie the mafic rocks of the ca. 2.056 Ga Rustenburg Layered Suite (Zeh et al.,
100 2015). The Zaaiplaats Sn deposit is located at approximately 24° 3'S, 28° 45'E, on the
101 northern limb of the Bushveld Complex, north-east of the town of Mokopane (Fig. 1).
102 The deposit is hosted by the Bobbejaankop and Lease granite bodies, both of which
103 fractionated from the voluminous underlying Nebo granite (McCarthy and Fripp, 1980;
104 Vonopartis et al., 2020), the principal component of the LGS.

105 The Bobbejaankop granite is a medium- to coarse-grained, orthoclase- and quartz-
106 rich, variably altered grey-red granite, whereas the overlying Lease granite is a thin (75
107 m), finer-grained aplite-like phase that caps the Bobbejaankop pluton (Coetzee and
108 Twist, 1989). The Zaaiplaats ore system has been interpreted to have developed as
109 the result of closed-system magmatic differentiation and the ensuing development of
110 a volatile fluid phase (Groves and McCarthy, 1978; Vonopartis et al., 2020). The bulk
111 of its Sn mineralization is found as low-grade disseminated cassiterite (SnO_2) within
112 the central mineralized zone of the Bobbejaankop body (Fig. 1A), where the whole-
113 rock Sn concentrations increase from 2-5 ppm along its margins to values as high as
114 350 ppm in the central mineralized zone (Coetzee and Twist, 1989). Higher grades of
115 Sn mineralization occur in the sericitized and reddened upper portions of the
116 Bobbejaankop and Lease units (Bailie and Robb, 2004; Pollard et al., 1989). This
117 reddening reflects a dusting of fine-grained hematite within the K-feldspar, whereas
118 sericitization tracks the emergence of a magmatic-hydrothermal fluid. The highest
119 grades of Sn ore occur in black pipe-like features (Fig. 1D), comprising sericitized
120 feldspar, chlorite, tourmaline, fluorite, and cassiterite, found within highly-altered
121 Bobbejaankop and Lease granites, that define the conduits where hydrothermal fluids
122 were focused into the upper portions of the system during the later stages of
123 crystallization.

3. Samples and Analytical Methodology

3.1. Samples

Nine samples were taken from a top to bottom section of the Zaaiplaats deposit, representing a transect across the magmatic-hydrothermal paragenesis (Fig. 1B; Table 1). Most of the samples are from two drill cores which intersect the Lease and Bobbejaankop granites, and one was from a surface pipe cropping out at the top of the Bobbejaankop granite (as in Fig. 1D).

We distinguish between granite samples that remain unaltered, and those that are altered and subject to incipient magmatic-hydrothermal mineralization processes, which focused fluid flow upwards into discrete pipe- or vug-related features containing abundant cassiterite (e.g., Fig. 1D). Samples are classified into three types: (i) unmineralized and unaltered grey granite; (ii) altered, reddened granite, which in hand specimen shows pervasive K-feldspar reddening and sericitization; (iii) mineralized samples from the central mineralized zone with obvious disseminated cassiterite and significantly elevated whole-rock Sn contents (Table 1). We also sampled a cassiterite-rich pipe (ZA1/9).

3.2. Zircon trace element analytical methodology

Approximately 1 kg of each sample was cleaned of surface contamination with compressed air and a wire brush prior to being crushed in a ceramic jaw crusher and milled in a tungsten carbide ring mill. The milled material was sieved with disposable nylon mesh, and the 63—118 μm and 118—250 μm fractions were placed in separate 500 ml beakers and washed repeatedly with water to remove clay particles before being left to dry overnight in an oven at 80 °C. The dried material from the two size fractions for each sample were passed through a Frantz isodynamic magnetic separator configured with a forward tilt of 25°, a side tilt of 15°, and a magnetic field

149 strength of 0.4 A to remove highly magnetic grains. A second pass with a field strength
150 of 1.40 A removed the remaining mild to weakly magnetic material (i.e., most
151 ferromagnesium minerals). The non-magnetic fraction from the 1.40 A pass for each
152 sample was selected for density separation using Diiodomethane heavy liquid (3.33
153 g/cm^3). The dense zircon-rich fraction was collected in filter paper, washed repeatedly
154 with acetone, and left to dry. The dried material was then poured onto doubled sided
155 tape cast into 1-inch round epoxy mounts.

156 The mounts were cured and polished to a 1 µm diamond finish and carbon coated.
157 Cathodoluminescence (CL) images of zircons (Appendix Figure A1) were collected
158 using a Phillips FEI XL30 environmental scanning electron microscope equipped with
159 a Gatan PanaCL panchromatic CL detector housed at the University of Melbourne,
160 Australia. The carbon coat was removed from the mounts using a cloth polishing lap
161 and 1 µm diamond paste, prior to laser ablation analysis. Targets for the laser ablation
162 analysis were selected on the basis of a range of cores and rims, zircon morphology
163 and clean versus altered domains, to analyze a range of zircon grains and domains.

164 Laser ablation analyses were carried out over two sessions (Dec 2018 and Jan 2020)
165 at the Isotopia Laboratory, School of Earth Atmosphere and Environment, Monash
166 University, Melbourne, using a Resonetics RESOlution-SE 193 nm Excimer Laser
167 ablation system with the ablated material split evenly between a Thermo iCAP TQ
168 ICPMS for U-Pb isotopic analysis and a Thermo iCAP RQ ICPMS for trace elements.
169 The aerosol produced during ablation was carried to the mass spectrometers via an
170 Ar–He mixture. A 30 µm spot size was used for all analyses, with the laser repetition
171 rate set to 10 Hz, with a fluence of approximately 4.5 J/cm^2 measured at the sample.
172 The elements measured were: ^{29}Si, ^{39}K, ^{43}Ca, ^{49}Ti, ^{51}V, ^{57}Fe, ^{60}Ni, ^{63}Cu, ^{66}Zn, ^{88}Sr, ^{89}Y,
173 ^{91}Zr, ^{93}Nb, ^{98}Mo, ^{109}Ag, ^{118}Sn, ^{139}La, ^{140}Ce, ^{141}Pr, ^{146}Nd, ^{147}Sm, ^{153}Eu, ^{157}Gd, ^{159}Tb, ^{163}Dy,
174 ^{165}Ho, ^{166}Er, ^{169}Tm, ^{172}Tb, ^{175}Lu, ^{178}Hf, ^{181}Ta, ^{182}W. Dwell times of 10 ms were used for

175 the more abundant elements (e.g., Si, Zr, Nb, etc) while for the lower abundance
176 elements, including Sn, dwell times of 20 ms were used.

177 All analyses were calibrated using internal standardisation to ^{29}Si with the glass NIST
178 610 as the primary reference material, using the Trace Element DRS of the Iolite data
179 reduction software. Internal standardization for trace elements assumed a ^{29}Si
180 concentration of 15.20 wt.% in zircon, and used accepted values for the glass
181 standards. Glass standards NIST 612, BHVO2G and BCR2G glasses as well as zircon
182 standards Plešovice, GJ1, and 91500, were run to assess data quality, with measured
183 values within error of accepted values (Appendix Table A1), and Sn (in BCR2G and
184 BHVO2G) is within 20% of accepted values.

185 In assigning errors to the measured Sm/Gd and Sn/Gd ratios, we calculated the
186 standard deviation of Sm/Gd and Sn/Gd in primary standard glass NIST 610,
187 secondary standard glass NIST 612, and secondary standard zircon Plešovice. For
188 Sm/Gd these gave 2σ uncertainties of: 1.5 %, 1.5 % and 6.8 % (610, 612 and Plešovice
189 respectively), and for Sn/Gd: 7.9 %, 7.5 % and 14.5 %. To be conservative, we
190 assigned 2σ uncertainties of 7 % to all Sm/Gd datapoints, and 15 % to all Sn/Gd
191 datapoints.

192 ## 4. Results

193 Sn could be measured in all the zircons analyzed, with concentrations varying from ~1
194 to 445 ppm (full results in Appendix Table A2). Figure 2 plots zircon Sn, Cu, Mo, W,
195 Sm, Ti, Y, and Nb versus zircon Gd for all Zaaiplaats samples, colour-coded by type –
196 unaltered, altered, and mineralized. Gd is used as a measure of fractionation in
197 Zaaiplaats zircons, because of the range in Gd contents (50-1500 ppm), the tight Gd-
198 Sm array, and because Gd covaries with Nb which increases with fractionation in the
199 whole rocks (Figs. 2 & 4).

Strikingly, for Sn and Cu in zircon the data fall along two trends. The zircons from samples classified as mineralized on the basis of their petrography have higher Sn and Cu contents compared to those from unmineralized samples at similar Gd contents; the zircons from samples classified as altered tend to have intermediate Sn contents and relatively low Gd contents, and mostly plot with the unmineralized samples (Fig. 2). In contrast to Sn and Cu, Mo and W show no resolvable difference between samples. Rare earth element (REE) patterns (Fig. 3) show enrichment in the heavy REE and Y, over the light REE, typical of igneous zircon (Belousova et al., 2002), and a pronounced Eu anomaly. The measured REE and Ti contents in the zircons record a range of abundances from low values (<10 ppm) to values higher than those typically reported from zircon in igneous rocks (Belousova et al., 2002; Burnham, 2020).

5. Discussion

5.1. Whole rock and zircon trace element trends

Figure 4A shows a plot of whole-rock Nb versus a differentiation index (TEDI) for the three granite units which make up the LGS, namely the Nebo, Bobbejaankop, and Lease phases (Kleemann and Twist, 1989; Labuschagne, 2004; Vonopartis et al., 2020). TEDI is a trace element discrimination index, defined as [(Ba x Sr)/Rb] that is used as a fractionation proxy in rock suites such as the LGS (Bailie and Robb, 2004; Walraven, 1982). Also plotted are whole-rock data for samples 46/8 and 47/10 (red triangle and grey box respectively), both taken from drill core through the Bobbejaankop granite. The whole-rock data show that Nb increases with decreasing TEDI (i.e. increasing fractionation), supporting the Nebo suite as being the parental granite to the Bobbejaankop and Lease units (McCarthy and Fripp, 1980).

A key step in evaluating the zircon record is how the elemental abundances measured in zircon, and in melts calculated to have been in equilibrium with zircon, compare with

the whole rock data. In practice, the zircon samples and the whole rock samples illustrate trends that represent very different scales. The whole rock data are for samples from across all three limbs of the LGS (Western, Eastern and Northern, covering some 30,000 km^2) whereas the zircons were taken from cores drilled 10's of metres apart on the Zaaiplaats property itself. Further, the calculated elemental abundances for magmas in equilibrium with zircon represent those present in the melts from which the zircons crystallized, whereas the whole rock granite sample compositions likely represent mixtures of both melt and cumulate crystals (McCarthy and Hasty, 1976).

Figure 4B plots whole-rock Y versus Nb, together with the calculated melt compositions in equilibrium with the zircons for the two samples for which whole-rock data are available – 46/8 and 47/10. The calculations were based on partition coefficients of $Kd_{zcn\text{-}melt}$ = 25 for Y (Gudelius et al., 2020; Pettke et al., 2005), and $Kd_{zcn\text{-}melt}$ = 1 for Nb, the latter within the range (0.15–2.2) quoted by Gudelius et al. (2020) and Nardi et al. (2013). Y increases with increasing Nb in the whole rocks, and also in the melts calculated to be in equilibrium with the zircons, indicating that Y increases with increasing fractionation.

The Zaaiplaats granites are highly fractionated and REE enriched. The Zaaiplaats zircon chemistry reflects this, and is similar to other highly evolved granites that also preserve elevated REE contents in zircon (e.g., Belousova et al., 2002; Pettke et al., 2005). Gd measured in zircon ranges from ~50–1500 ppm, while the whole-rock contents vary from 7–1860 ppm. A Gd $Kd_{zcn\text{-}melt}$ = 10 provides a good fit for the melts in equilibrium with the zircons with the whole-rock data, and accords with the ranges (3–27) reported for similar granite systems by Nardi et al. (2013) as well as those from melt inclusions in zircons from other felsic units of the Bushveld described by Gudelius et al. (2020).

Figure 4C plots whole-rock Y versus Gd as well as melt compositions in equilibrium with the zircons in samples 46/8 and 47/10, using a $Kd_{zcn\text{-}melt}$ = 10 for Gd, and $Kd_{zcn\text{-}melt}$ = 25 for Y. In both the whole-rock and zircon melt data, Y increases with both Gd and Nb (Fig. 4B), and Nb has been shown to increase with decreasing TEDI and increasing fractionation (Fig. 4A). Coherent Gd–Sm–Sn trends are observed in the zircons (Fig. 2), and Gd is therefore an index of differentiation in the Zaaiplaats zircon archive. Overall, the whole-rock data tend to be less evolved than the melts in equilibrium with the zircons, and the zircon melts from the unmineralized samples (e.g., 46/8) range to higher degrees of fractionation than those in the mineralized samples (e.g., 47/10).

Under some circumstances, incompatible elements in zircon can be remobilized, potentially disturbing primary magmatic signatures (Burnham, 2020; Geisler et al., 2007). Cathodoluminescence (CL) images of the analyzed zircons (Appendix Figure A1) show that whereas many exhibit magmatic growth zoning, there is evidence in some crystals for a degree of hydrothermal overprinting, including convolute zoning, micro veinlets, and homogeneous dark patches and rims. Some of our analyses were from these domains, but no relationship was observed between elevated zircon REE and altered portions of the grains as indicated by dark CL response.

Later fluid-related overprinting of zircon may also be monitored by “non-stoichiometric” non-lattice bound elements, such as Ca, Fe, and Al. These elements can be involved in substitution during magmatic zircon growth (Hoskin et al., 2000), but they are potentially mobile during later alteration, resulting in elevated and variable values that are independent of any magmatic signature (Geisler et al., 2007). In such cases Ca, Fe, and Al abundances should not follow trends linked to magmatic fractionation. At a whole-rock level, Ca, and to a lesser extent Fe, increase with the REE and thus with magmatic fractionation in the Zaaiplaats granites (Vonopartis et al., 2020). Plotting zircon Ca versus Gd (Fig. 5A) shows a scatter displaced to relatively low Ca values at particular Gd contents, which implies disturbance of an original magmatic trend, and a

278 degree of decoupling between Ca (and Fe) and the REEs. This decoupling contrasts
279 with the well-defined zircon inter-REE trends such as Gd versus Sm (Fig. 2E) observed
280 in all samples, including those displaying pervasive reddish alteration in hand-
281 specimen (classified here as both altered and mineralized). Plotting zircon Sn versus
282 Ca (Fig. 5B) shows reasonable, albeit different, positive arrays in the mineralized and
283 unmineralized samples, which implies that elevated Sn observed in the mineralized
284 samples is not associated with concomitant enrichment in Ca, and is similar to the
285 trends in Sn versus Gd (e.g., Fig. 5C). Taken together, we interpret these trends as
286 signifying that (a) there was some later (post-magmatic) alteration which partially
287 disturbed Fe and Ca; and (b) the Zaaiplaats zircons REE and Sn profiles were not
288 significantly disturbed by this later hydrothermal metasomatism.

289 Plotting zircon Sm/Gd versus Pr/Yb (Fig. 5D) shows similar trends for both mineralized
290 and unmineralized samples, with the implication that both sets of samples recorded
291 similar REE fractionation processes. Thus, the variations in REE and HFSE in zircon
292 (e.g. Gd–Sm, Gd–Nb, Pr/Yb–Sm/Gd), which reflect consistent REE normalized profiles
293 (Fig. 3) and compare well with the whole-rock fractionation trends, indicate that the
294 zircon REE profiles were not significantly disturbed by mineralization or subsequent
295 alteration and that they represent robust magmatic signatures.

296 Plots of Sn and Cu versus Gd in the zircons (Fig. 2A, B) show, however, that both Sn
297 and Cu are elevated in the mineralized samples over the unmineralized samples, but
298 that this is not the case for Gd. This highlights that the processes that resulted in
299 elevated transition metal (Sn and Cu) contents in the zircons of the mineralized
300 samples did not result in higher concentrations of REE. Thus, even in the altered and
301 mineralized samples the REE largely represent magmatic signatures and they remain
302 largely unaffected by the processes giving rise to Sn and Cu enrichment.

The Zaaiplaats zircons have concentrations of Ti and REE higher than those typically reported from zircons in arc-type systems (cf. Burnham, 2020). We argue the Zaaiplaats zircon trace element concentrations reflect zircon crystallization in systems which are REE enriched and have already undergone significant magmatic fractionation. The Bobbejaankop host granite has whole-rock Ti contents of the order of 200–1600 ppm (Vonopartis et al., 2020) and it does not contain other common Ti bearing phases; ilmenite, rutile and sphene are mainly absent, as is biotite. Published zircon-melt *Kd* values for Ti range by up to the order of 3 (e.g. Luo and Ayers, 2009). Thus, the zircon Ti contents of the 100's ppm are considered to reflect Ti partitioning into zircon in the absence of other Ti-hosting phases, and that Ti is incompatible. Belousova et al. (2002) reported similar zircon Ti concentrations (500–700 ppm) from Eastern Australian granites. Such elevated Ti concentrations clearly have implications for utility of the Ti-in-zircon thermometer (Watson et al., 2006) to similar evolved systems, since that tool relies upon the co-existence of other Ti-bearing phases, and it would not be applicable here.

5.2. Modelling Rayleigh Fractionation

A magmatic system following closed system crystal fractionation, such as that represented by the LGS granites (Groves and McCarthy, 1978; Vonopartis et al., 2020), will exhibit trace element variations that approximate Rayleigh Fractionation. Assuming that the REE zircon trends represent magmatic fractionation processes unaffected by mineralization processes or later alteration, they have been modelled in terms of Rayleigh Fractionation of the host magma from which the zircons crystallized. Neodynium and O isotopes measured in the Nebo granite, considered to be the parental melt to the Bobbejaankop granite, have typical εNd values of ~ -5 and δ^{18}O of ~7 ‰, suggesting that this melt was derived from pre-existing crustal material (Fourie and Harris, 2011).

329 The Nebo granite is less evolved than the Bobbejaankop and Lease granites, and it is
330 taken to represent the parent magma (McCarthy and Fripp, 1980). As a starting point
331 for fractionation modelling, we took a modal mineralogical assemblage for the Nebo
332 granite (Appendix Table A4), and an initial bulk-rock composition approximating the
333 minimum Gd, Y and Sn contents of the ten least fractionated (highest TEDI) Nebo
334 samples, illustrated in Figure 4A. This starting composition has X_{Gd} = 25 ppm, X_Y = 20
335 ppm, X_{Sn} = 2 ppm, a SiO_2 content of approximately 71 wt.% and Rb/Sr of 0.8. Using
336 the modal assemblage, we calculated bulk *D* values for the elements of interest
337 (Appendix Table A5), by multiplying individual mineral-melt *Kd* values by their mode.

338 We applied the Rayleigh Fractionation equation to model residual melt Gd contents as
339 the putative Bobbejaankop melt crystallizes. We then applied the previously used
340 $Kd_{zcn\text{-}melt}$ values to the calculated residual melt compositions to derive the trace element
341 contents of zircon crystallizing in equilibrium with those melts. The calculated contents
342 of Gd in zircon range over 3000 ppm, and readily accommodate the range of measured
343 values (50–1500 ppm), with the higher values representing the more highly
344 fractionated melts.

345 In summary, the Bobbejaankop and Lease granite units represent highly evolved A-
346 type granitic systems. The melts in equilibrium with zircon range to more fractionated
347 compositions than the whole rocks (e.g., Fig. 4B, 4C), and the zircons are
348 characterized by unusually high concentrations of, for example, REE, Y and Ti.

349 5.3. *Zaaiplaats magma fractionation trend*

350 The incompatible elements Sm, Gd and Y are all measures of magma fractionation in
351 felsic systems such as Zaaiplaats (Fig. 2E and Belousova et al., 2002), and they
352 behave similarly following Rayleigh Fractionation trends. Thus, ratios of these
353 elements in the melt, such as Sm/Gd, are expected to change little with fractional
354 crystallization. These elements have similar zircon-melt partition coefficients, and their

355 relative abundances are not expected to change significantly across the range of
356 magma fractionation at Zaaiplaats; zircon Sm/Gd will therefore reflect the evolving melt
357 Sm/Gd, and it should likewise change little with fractional crystallization.

358 Figure 6A plots zircon Sm/Gd versus zircon Y measured in the same laser ablation
359 spots. Unmineralized, altered, and mineralized samples have similar zircon Sm/Gd
360 across their range in Y (500 to 20,000 ppm; Fig. 6A), and all samples, whether
361 mineralized or not, have similar REE fractionation patterns (Figure 3) with the
362 implication that: (i) Sm/Gd is unaffected by mineralization processes; and (ii) all
363 samples are derived from similar parental magmas (cf. Vonopartis et al., 2020). We
364 take the array in zircon Sm/Gd versus Y as representing the Zaaiplaats magma
365 fractionation trend, along which the magmatic system evolved by crystal fractionation
366 processes and from which the zircons crystallized. This fractionation trend is annotated
367 in Figure 6A as the dashed blue line.

368 *5.4. Tracking mineralization processes*

369 The solubility of tin in granitic melts is complex and its behaviour is dependent on
370 magma composition, in particular peralkalinity, and the contrasting behaviour of Sn^{2+}
371 and Sn^{4+} (Farges et al., 2006). However, tin typically behaves incompatibly in granitic
372 melts (Heinrich, 1990) and, in most cases, abundances increase with progressive
373 crystallization, with cassiterite ultimately forming as a minor liquidus phase in the more
374 fractionated portions of the system. During magma crystallization and fractionation, Sn
375 should therefore behave in a similar fashion to Gd and the other REEs, and Sn/Gd
376 should remain constant with fractionation. Thus, assuming a constant $Kd_{zcn\text{-}melt}$ during
377 fractionation, zircons from the unmineralized samples plot in a horizontal array on a
378 plot of zircon Sn/Gd versus Y (Fig. 6B), and that defines the Zaaiplaats magma
379 fractionation trend, which we attribute to a magma system dominated by crystal
380 fractionation processes. In contrast to the unmineralized and altered samples, all the

zircons from the mineralized samples have Sn/Gd values displaced to higher values across their range in Y (Figs. 2 & 6B).

The trends that differentiate between unmineralized and mineralized samples (Figs. 2A-D) clearly show elevated Sn and Cu zircon contents in the mineralized samples at similar Gd. In contrast, Mo and W contents are indistinguishable, and it appears that in the Zaaiplaats magmatic system, both metals were effectively immobile during both mineralization (and later alteration), and reflect melt concentrations which we interpret as the product of magma fractionation. Rayleigh Fractionation, however, cannot account for the whole-rock Sn enrichment within the central Bobbejaankop mineralized zone (Coetzee and Twist, 1989), and the elevated zircon Sn and Cu contents recorded in these samples point to processes other than magma fractionation as being responsible for their elevated concentrations.

The Zaaiplaats fractionation array in the plot of Sn/Gd versus Y (Fig. 6B) provides a baseline against which related mineralization processes over those expected by ordinary magma fractionation alone may be referenced. The mineralization is reflected in elevated Sn/Gd and plotting log Sn versus log Gd in zircon (Fig. 6C) highlights an event of Sn enrichment that occurs relatively early in the fractionation history recorded by the zircons, and that fractionation continues after this point.

We therefore extended our Rayleigh Fractionation model to explore how Sn/Gd varies with magma fractionation when the Sn trend is disturbed by a process, such as the introduction of a Sn-rich fluid phase. Initially, we modelled the evolution of zircon Sn/Gd as a function of fractionation alone. There are limited published data for Sn in zircon, so we took $Kd^{Sn}_{zcn\text{-}melt} = 0.6$ (Pettke et al., 2005), which is consistent with the ranges of the minimum and maximum whole-rock (2 – 1685 ppm) and zircon (0.5 – 400 ppm) Sn contents (using the whole-rock data of Vonopartis et al. (2020)). This value for $Kd^{Sn}_{zcn\text{-}melt}$ is similar, albeit slightly lower, to values for the light REEs (Bea et al., 1994). Taking

407 the initial bulk rock composition as before, we applied the Rayleigh Fractionation
408 equation to model residual melt Sn/Gd as a function of Y, and converted this to zircon
409 Sn/Gd ratios in equilibrium with the residual melts (Figure 7).

410 Although the modelled concentrations of both Sn and Gd in the melt increase
411 exponentially with fractionation, Figure 7 shows that Sn/Gd in zircon is constant with
412 increasing Y (Fig. 7, blue line). Samples that plot at elevated zircon Sn/Gd are
413 displaced from this fractionation trend at a Y content of ~1900 ppm. We consider this
414 to effectively mark the onset of mineralization, i.e. the “mineralization step”, at
415 Zaaiplaats (Fig. 7, red arrow), and thus it defines the point during magma fractionation
416 at which zircons start to record excess Sn above that attributable to magma
417 fractionation alone. At this point the residual magma has a bulk Y content of 76 ppm,
418 which in our modelling corresponds to F ~0.14, or ~86 % crystallization.

419 To explore how zircon Sn/Gd is disturbed during the appearance of a Sn-rich fluid, we
420 then modelled its introduction after 86 % crystallization. We assumed that the fluid plus
421 residual magma co-exists, and that zircon continues to crystallize from the fluid-
422 saturated melt. The fluid-saturation event is marked in the field by vugs and tourmaline-
423 cassiterite-chlorite rich pipes that emanate from the more fractionated central portions
424 of the Bobbejaankop granite, and terminate towards its roof and into the Lease granite.
425 To the modelled system (at 86 % crystallization, or F = 0.14) we added additional Sn
426 to reflect its abundance in the mineralizing fluid. We considered a range of Sn contents
427 (10–5000 ppm) within the carrying capacity of such high-temperature volatile-rich fluids
428 (Audetat et al., 1998), and for a range of different fluid:melt ratios (1:4 to 1:100)
429 reflecting realistic fluid solubilities in magmas (Whitney and Naldrett, 1989), and
430 representing the addition of between 1–25 % fluid. This excess Sn was “added” to the
431 modelled fractionating melt at the mineralizing step, after which the melt continued to
432 fractionate according to Rayleigh Fractionation, and zircon continued to grow.
433 Assuming zircon grows in equilibrium with combined melt and fluid phase allowed us

434 to calculate a composite “melt + fluid” Sn composition, using the same $Kd^{Sn}_{zcn\text{-}melt}$ for
435 the magma plus fluid (e.g., Pettke et al., 2005) to calculate Sn/Gd in zircon for the
436 different scenarios (Appendix Table A6). The results from this modelling are seen in
437 Table 2, which shows calculated Sn/Gd at the mineralization step (F =0.14) as a
438 function of both fluid:melt ratio and fluid Sn content.

439 Most measured zircons within the mineralized samples record Sn/Gd in the range 0.05
440 to 0.35 across the range in Y after the mineralization step, and the red lines in Figure
441 7 model these upper and lower limits of zircon Sn/Gd and its continued fractionation in
442 the magmatic system after fluid saturation. The range in Sn/Gd (highlighted in green
443 in Table 2) defines a continuum between higher Sn contents in fluid at lower fluid:melt
444 ratios (e.g. 2000 ppm at 0.01), and lower Sn contents at higher fluid:melt ratios (e.g.
445 100 ppm at 0.2), to illustrate different scenarios by which similar Sn enrichment might
446 be achieved. Fluid inclusion data from the Yankee Tin Lode in the Mole granite of New
447 South Wales, suggests that typical Sn concentrations before cassiterite deposition
448 were around 400 ppm (Audetat et al., 1998) which, in terms of our modelling, would
449 suggest fluid:melt ratios in the range 0.05–0.3.

450 *5.5. Zaaiplaats mineralization model*

451 A crystallizing magma system such as Zaaiplaats will reach the point of volatile
452 saturation through decompression and/or crystal fractionation, leading to the
453 exsolution of a separate aqueous phase (Burnham, 1979). Under certain conditions,
454 this phase will contain volatile ligands (Cl, F) to which metals may bond, allowing it to
455 scavenge metals as it migrates through the residual melt, facilitating their
456 transportation and concentration (e.g., Burnham, 1997; Heinrich, 1990).

457 The Zaaiplaats hydrothermal system is thought to have been relatively long-lived.
458 Emplacement of the LGS was essentially coeval with, but immediately succeeded,
459 emplacement of the Rustenburg Layered Suite. This thick mafic underplating

460 represented a significant thermal anomaly and it maintained ongoing fluid circulation
461 perhaps over several million years (Robb et al., 2000). Fluid inclusion evidence
462 suggests two phases of hydrothermal fluids: (i) early, short-lived magmatically-derived
463 hot saline fluids, and; (ii) later, cooler, longer-lived less saline fluids derived by
464 progressive mixing of magmatic fluids with connate waters (Pollard et al., 1991a; Robb
465 et al., 2000). The Sn (and W) mineralization is thought to be linked to the early fluids
466 of magmatic-origin, consistent both with studies of the paragenetic sequence (Bailie
467 and Robb, 2004), and the likelihood that cassiterite would have precipitated out at
468 temperatures above 400^{o}C (Heinrich, 1990). The later fluid mixing event took place
469 substantially later than magma emplacement and cooling (possibly at circa 1950 Ma;
470 Robb et al., 2000); we see no evidence for this event having disturbed the zircon trends
471 in REE and HFSE.

472 The metals Sn and Cu are both readily soluble in Cl-rich aqueous hydrothermal fluids,
473 likely forming $SnCl_2$ and $CuCl_2$ complexes (Candela and Holland, 1984; Keppler and
474 Wyllie, 1991). In contrast, Mo typically only dissolves in high pH fluids as $Mo(OH)_2$
475 (Candela, 1992), and although W dissolves as H_2WO_4 in moderately to highly acidic
476 fluids (Wood and Samson, 2000), it may behave similarly to Mo (Candela, 1992). Thus,
477 a saline, acidic hydrothermal fluid will be capable of transporting and concentrating Sn
478 and Cu, but would be less capable of mobilising Mo and W. At Zaaiplaats, the presence
479 of such a hydrothermal fluid is implied by the pervasive alteration of the upper,
480 reddened Bobbejaankop granite, represented here by both altered and mineralized
481 samples, and in fluorite- and tourmaline- rich vugs and pipes (Ollila, 1981). The initial
482 hydrothermal system at Zaaiplaats was dominated by fluids of magmatic origin, with
483 little to no input of external meteoric water (effectively a closed system), and fluid
484 inclusions linked to this early system have significant concentrations of Cl and F,
485 consistent with a highly saline fluid (Ollila, 1981; Pollard et al., 1991a). This fluid also

appears to have been acidic, as evidenced by the host rock sericitization (Pollard et al., 1991a).

In the preferred model for Zaaiplaats, elevated Sn and Cu contents in the mineralized samples reflect the exsolution of a magmatically-derived, acidic, volatile-rich hydrothermal fluid that has significantly concentrated available Sn via migration through the residual melt in the pluton. The Zaaiplaats granites preserve whole-rock Sn zonation consistent with such closed-system magma differentiation and the ensuing exsolution of an acidic, saline, metal-rich magmatic-hydrothermal fluid (Groves and McCarthy, 1978; Pollard et al., 1991b; Robb et al., 2000). This process led to the development of Sn mineralization in the fractionated central Bobbejaankop granite, both as disseminated cassiterite and in focused in cassiterite–tourmaline pipes, as well as being responsible for the pervasive reddening and alteration of the host granite. We interpret this mineralization process as being reflected in zircon Sn/Gd ratios that are elevated above those of the fractionation trend in Figure 6B, representing zircon growth from the magma after the introduction of a Sn-rich fluid phase and which marked the onset of mineralization processes. Elevated Sn values were measured in the cores of zircons as well as the rims, implying early and ongoing zircon growth in the presence of these metal-rich fluids, and all the zircons from any one sample plot within the same trends, whether mineralized or not. We suggest that the addition of excess Sn represents a single event after which melt plus fluid fractionated along the mineralized trends represented by the red lines in Figure 7. We prefer the concept of a single input of additional Sn into the melt system, to that of continuous Sn addition during fractionation. In the latter scenario, keeping Sn/Gd constant would imply that the amounts of Sn being introduced to the system increased in-line with fractionation, which we consider unlikely.

5.6. Comparison to earlier work

The ubiquity of zircon in evolved rocks has led to investigations into how its chemistry may reflect the development of magmatic-hydrothermal mineral deposits. Zircon REE contents, in particular the utility of Ce anomalies as a proxy oxybarometer, have been studied as pathfinders primarily for Cu mineralization potential (Ballard et al., 2002; Dilles et al., 2015; Lu et al., 2016; Shen et al., 2015). Coupled application of zircon Eu and Ce anomalies have been shown to distinguish between Cu and Sn-hosting granites (Gardiner et al., 2017; Li et al., 2019). Focusing on complex polymetallic deposits, Li et al. (2014) used zircon REE, Ti, and Hf contents to discriminate between magmatic versus hydrothermally-derived zircon, linking these to zircon U–Pb ages to assess the relative timing of mineralization events. These authors showed that in their study area Cu (Pb-Zn) mineralization was associated with early granophyric magmas, whilst later W-Sn mineralization with more evolved granite porphyritic intrusions. Similarly, Jiang et al. (2020) applied trace elements and Hf isotopes in zircon taken from a polymetallic deposit to identify those which have interacted with metal-rich hydrothermal fluids, and to assess the nature of those fluids.

In this study we take a different approach. We specifically target those metals of economic interest within zircon sampled from a well-characterized mineralized system, and assess how the zircon metal contents may reflect the genesis of the deposit. We show that metals such as Sn, Cu, W, and Mo can be reliably measured within zircon, and that coupled with a proxy for the evolution of the magmatic system (here, Gd and Y), how their concentrations might reflect the introduction of a mineralizing fluid and hence the processes of mineralization, as monitored via metal anomalies.

5.7. Implications for the genesis of tin deposits

Recent experimental work by Schmidt et al. (2020) focused on the role of Sn and W during volatile saturation in S-type granite systems. Their data showed that Sn

preferentially partitioned into the melt over the hydrothermal fluid, whereas by contrast W had a strong affinity for the fluid. The implications of this are potentially highly significant and contradict classic models of tin metallogeny (e.g., Heinrich, 1990), suggesting that during volatile saturation Sn remains within the melt, and it is therefore the melt and not hydrothermal fluids which is the main source of Sn for mineralization processes. Our zircon data appear to contradict these findings. We interpret the pipe- and vug-hosted tin mineralized zone at Zaaiplaats to have resulted from an input of additional Sn over that provided by magmatic fractionation processes alone, and for this to have been delivered by saline hydrothermal fluids. Thus, at Zaaiplaats, it is the addition of excess Sn via hydrothermal fluids that drives the formation of economically-viable mineralization. Further, we find W and the REE to be relatively immobile, with the implication that they were not concentrated to any extent into the hydrothermal fluid phase at Zaaiplaats. This stands in contrast to the results of Schmidt et al. (2020), suggesting that the difference in W mobility is likely to be a function of different fluid chemistry and acidity.

5.8. Metal anomalies and wider implications

In nickel ore deposits formed from mafic rocks, the Ni anomaly (Ni/Ni*) describes the extent to which olivine-hosted Ni concentration is depleted by the appearance of an immiscible, Ni-sequestering sulphide phase, relative to that expected for olivine (silicate) fractionation alone (Naldrett, 1989). A similar concept is developed here for magmatic-hydrothermal systems based on measurable metal contents in an evolving granite system.

The Zaaiplaats study here defines the tin anomaly, Sn/Sn*, as the deviation of Sn, preferentially sequestered by a fluid phase, from that expected in the magmatic system alone (Sn*), in this case measured using Sn/Gd (Fig. 7). Importantly, such deviations occur during mineralization associated with volatile (rather than sulphide) saturation,

563 and thus Sn/Sn* may be used to fingerprint this process. In our model, the observed
564 displacement of zircon Sn/Gd above the fractionation trend represents the
565 development of elevated Sn/Sn* in the zircon archive of the Zaaiplaats samples. We
566 suggest that a measurable and resolvable Sn/Sn*, whether in mineral archives or in
567 whole-rocks, marks the onset of volatile saturation with accompanying concentration
568 of metals from the residual magma, and ultimately the precipitation of ore minerals.

569 We further propose that the concept of metal anomalies applied to magmatic-
570 hydrothermal systems – at the mineral or whole-rock level – can be extended for other
571 metal enrichments, for example Cu/Cu*. This concept has utility at Zaaiplaats, which
572 records Cu mineralization (Appendix Figure A2), and may also be applicable to
573 magmatic-hydrothermal systems in arc-related settings.

574 6. Conclusions

575 We demonstrate that the chemistry of zircons, in this case from a profile across the
576 Zaaiplaats granites, may be used to distinguish between the processes of magma
577 fractionation and the concentration of metals associated with magmatic-hydrothermal
578 mineralization. Mineralization at the Zaaiplaats Tin Field lies in the Lebowa Granite
579 Suite of the Bushveld Complex, and it resulted from closed-system fractionation and
580 the eventual appearance of a Sn-rich hydrothermal fluid of magmatic origin which
581 promoted cassiterite precipitation in the mineralized zone.

582 Our study uses unmineralized samples as the benchmark to define a fractionation
583 trend on the basis of zircon REE and HFSE arrays, where Sn content is dominated by
584 Rayleigh Fractionation. Deviation from this trend is represented by a significant
585 enrichment of Sn, and it marks the introduction of a Sn-rich fluid resulting from volatile
586 saturation and the onset of mineralization processes. In the preferred model, the
587 deviation is explained by introduction at an advanced stage (> 85 %) of crystallization,

588 of a significant volume of co-existing exsolved fluid that has concentrated Sn to levels
589 of up to 400 ppm. This model is consistent with the notion that crystal fractionation
590 accompanied by addition of Sn via a fluid phase is required to create a mineralized tin
591 granite such as that found at Zaaiplaats. However, at Zaaiplaats, without the formation
592 of conduits, such as the pipes to focus the fluids, it is unlikely that an economically
593 viable deposit would have formed.

594 Identification of metal anomalies – Sn/Sn* and, more widely Cu/Cu* – in mineral
595 archives or at the whole-rock level, provides an empirical link to the onset of
596 mineralization processes in magmatic-hydrothermal systems. Metal anomalies can be
597 coupled with geochemical proxies for source, redox, and other attributes, to yield a
598 better understanding of the conditions leading up to, and subsequent to, volatile
599 saturation, resulting eventually in the development of potentially economically viable
600 mineralization. Ultimately, identification of metal anomalies can be developed into
601 exploration tools that will assist with the identification of systems that have experienced
602 magmatic-hydrothermal mineralization processes.

603 ## Acknowledgements

604 Funding: This work was supported by Australian Research Council grant
605 FL160100168 (NJG, ANW, JAM, and PAC); Leverhulme Trust RPG-2015-422 and
606 EM-2017-047\4 (CJH). This work forms a contribution to the THRIP Project “Using
607 mineral chemistry to identify base and precious metal mineralization in the Bushveld
608 Complex” at the University of the Witwatersrand. LJR acknowledges the support of the
609 DSI-NRF Centre of Excellence for Integrated Mineral and Energy Resource Analysis
610 (DSI-NRF CIMERA), at the University of Johannesburg, towards this research. We thank
611 Balz Kamber for editorial handling and useful reviews from two anonymous reviewers.

612 # References

613 Audetat, A., Gunther, D., Heinrich, C., 1998. Formation of a Magmatic-
614 Hydrothermal Ore Deposit: Insights with LA-ICP-MS Analysis of Fluid
615 Inclusions. Science, 279(5359): 2091-2094.

616 Bailie, R.H., Robb, L.J., 2004. Polymetallic mineralization in the granites of the
617 Bushveld Complex – examples from the central southeastern lobe.
618 South African Journal of Geology, 107: 633-652.

619 Ballard, J.R., Palin, M.J., Campbell, I.H., 2002. Relative oxidation states of
620 magmas inferred from Ce(IV)/Ce(III) in zircon: application to porphyry
621 copper deposits of northern Chile. Contributions to Mineralogy and
622 Petrology, 144(3): 347-364.

623 Bea, F., Pereira, M.D., Stroh, A., 1994. Mineral/leucosome trace-element
624 partitioning in a peraluminous migmatite (a laser ablation-ICP-MS
625 study). Chemical Geology, 117: 291-312.

626 Belousova, E., Griffin, W., O'Reilly, S.Y., Fisher, N., 2002. Igneous zircon: trace
627 element composition as an indicator of source rock type. Contributions
628 to Mineralogy and Petrology, 143(5): 602-622.

629 Blevin, P.L., Chappell, B.W., 1992. The role of magma sources, oxidation states
630 and fractionation in determining the granite metallogeny of eastern
631 Australia. Transactions of the Royal Society of Edinburgh: Earth
632 Sciences, 83: 305-316.

633 Blundy, J., Mavrogenes, J., Tattitch, B., Sparks, S., Gilmer, A., 2015.
634 Generation of porphyry copper deposits by gas–brine reaction in
635 volcanic arcs. Nature Geoscience, 8(3): 235-240.

636 Burnham, A.D., 2020. Key concepts in interpreting the concentrations of the
637 rare earth elements in zircon. Chemical Geology, 551.

638 Burnham, C.W., 1979. Magmas and hydrothermal fluids. In: Barnes, H.L. (Ed.),
639 Geochemistry of Hydrothermal Ore Deposits. John Wiley & Sons, pp.
640 71-136.

641 Burnham, C.W., 1997. Magmas and hydrothermal fluids. In: Barnes, H.L. (Ed.),
642 Geochemistry of Hydrothermal Ore Deposits. John Wiley & Sons, pp.
643 71-136.

644 Candela, P.A., 1992. Controls on ore metal ratios in granite-related ore
645 systems: an experimental and computational approach. Transactions of
646 the Royal Society of Edinburgh: Earth Sciences, 83(1-2): 317-326.

647 Candela, P.A., 1997. A Review of Shallow, Ore-related Granites: Textures,
648 Volatiles, and Ore Metals. Journal of Petrology, 38(12): 1619-1633.

649 Candela, P.A., Holland, H.D., 1984. The partitioning of copper and molybdenum
650 between silicate melts and aqueous fluids. Geochimica et
651 Cosmochimica Acta, 48: 373-380.

652 Černý, P., Blevin, P.L., Cuney, M., London, D., 2005. Granite-related ore
653 deposits. Economic Geology 100th Anniversary Volume: 337-370.

654 Chelle-Michou, C., Rottier, B., Caricchi, L., Simpson, G., 2017. Tempo of
655 magma degassing and the genesis of porphyry copper deposits.
656 Scientific Reports, 7: 40566.

657 Coetzee, J., Twist, D., 1989. Disseminated Tin Mineralization in the Roof of the
658 Bushveld Granite Pluton at the Zaaiplaats Mine, with Implications for the
659 Genesis of Magmatic Hydrothermal Tin Systems. Economic Geology,
660 84: 1817-1834.

661 Dilles, J.H. et al., 2015. Zircon compositional evidence for sulfur-degassing
662 from ore-forming magmas. Economic Geology, 110: 241-251.

663 Duc-Tin, Q., Audétat, A., Keppler, H., 2007. Solubility of tin in (Cl, F)-bearing
664 aqueous fluids at 700°C, 140MPa: A LA-ICP-MS study on synthetic fluid
665 inclusions. Geochimica et Cosmochimica Acta, 71(13): 3323-3335.

666 Farges, F., Linnen, R.L., Brown, G.E., 2006. Redox and Speciation of tin in
667 hydrous silicate glasses: A comparison with Nb, Ta, Mo and W.
668 Canadian Mineralogist, 44(3): 795-810.

669 Fourie, D.S., Harris, C., 2011. O-isotope Study of the Bushveld Complex
670 Granites and Granophyres: Constraints on Source Composition, and
671 Assimilation. Journal of Petrology, 52(11): 2221-2242.

672 Gardiner, N.J. et al., 2017. Contrasting Granite Metallogeny through the Zircon
673 Record: A Case Study from Myanmar. Scientific Reports, 7(1): 748.

674 Geisler, T., Schaltegger, U., Tomaschek, F., 2007. Re-equilibration of Zircon in
675 Aqueous Fluids and Melts. Elements, 3(1): 43-50.

676 Groves, D.I., McCarthy, T.S., 1978. Fractional crystallization and the origin of
677 tin deposits in granitoids. Mineralium Deposita, 13: 11-26.

678 Gudelius, D. et al., 2020. Zircon melt inclusions in mafic and felsic rocks of the
679 Bushveld Complex – Constraints for zircon crystallization temperatures
680 and partition coefficients. Geochimica et Cosmochimica Acta, 289: 158-
681 181.

682 Hart, C.J.R., Mair, J.L., Goldfarb, R.J., Groves, D.I., 2004. Source and redox
683 controls on metallogenic variations in intrusion-related ore systems,
684 Tombstone-Tungsten Belt, Yukon Territory, Canada. Transactions of the
685 Royal Society of Edinburgh: Earth Sciences, 95: 339-356.

686 Hedenquist, J.W., Lowenstein, J.B., 1994. The role of magmas in the formation
687 of hydrothermal ore deposits. Nature, 370: 519-527.

688 Heinrich, C., 1990. The Chemistry of Hydrothermal Tin (-Tungsten) Ore
689 Deposition. Economic Geology, 85: 457-481.

690 Heinrich, C., Gunther, D., Audetat, A., Ulrich, T., Frischknecht, R., 1999. Metal
691 fractionation between magmatic brine and vapor, determined by
692 microanalysis of fluid inclusions. Geology, 27: 755-758.

693 Hoskin, P.W.O., 2003. The Composition of Zircon and Igneous and
694 Metamorphic Petrogenesis. Reviews in Mineralogy and Geochemistry,
695 53(1): 27-62.

696 Hoskin, P.W.O., Kinny, P.D., Wyborn, D., Chappell, B.W., 2000. Identifying
697 accessory mineral saturation during differentiation in granitoid magmas:
698 an integrated approach. Journal of Petrology, 41(9): 1365-1396.

699 Jiang, W.-C., Li, H., Turner, S., Zhu, D.-P., Wang, C., 2020. Timing and origin
700 of multi-stage magmatism and related W–Mo–Pb–Zn–Fe–Cu
701 mineralization in the Huangshaping deposit, South China: An integrated
702 zircon study. Chemical Geology, 552.

703 Kemp, A.I., Hawkesworth, C., 2013. Granitic Perspectives on the Generation
704 and Secular Evolution of the Continental Crust. Treatise on
705 Geochemistry: 349-421.

706 Keppler, H., Wyllie, P.J., 1991. Partitioning of Cu, Sn, Mo, W, U, and Th
707 between melt and aqueous fluid in the systems haplogranite-H2O−HCl
708 and haplogranite-H2O−HF. Contributions to Mineralogy and Petrology,
709 109: 139-150.

710 Kleemann, G.J., Twist, D., 1989. The compositionally-zones sheet-like granite
711 pluton of the Bushveld Complex: Evidence bearing on th nature of A-
712 type magmatism. Journal of Petrology, 30: 1383-1414.

713 Labuschagne, L.S., 2004. Evolution of the ore-forming fluids in the Rooiberg tin
714 field, South Africa. Memoir, 96. Council for Geoscience (South Africa),
715 Pretoria.

716 Li, H., Watanabe, K., Yonezu, K., 2014. Zircon morphology, geochronology and
717 trace element geochemistry of the granites from the Huangshaping
718 polymetallic deposit, South China: Implications for the magmatic
719 evolution and mineralization processes. Ore Geology Reviews, 60: 14-
720 35.

721 Li, X., Gao, Q., Song, H., Chi, G., Lai, C.-K., 2019. Discriminating ore fertile and
722 barren granites using zircon Ce and Eu anomalies – Perspective from
723 late Mesozoic (Yanshanian) granites in South China. Ore Geology
724 Reviews, 113.

725 Lu, Y.J. et al., 2016. Zircon Compositions as a Pathfinder for Porphyry Cu ± Mo
726 ± Au Deposits. Economic Geology Special Publication 19: 329-347.

727 Luo, Y., Ayers, J.C., 2009. Experimental measurements of zircon/melt trace-
728 element partition coefficients. Geochimica et Cosmochimica Acta,
729 73(12): 3656-3679.

730 McCarthy, T.S., Fripp, R.E.P., 1980. The crystallization history of a granitic
731 magma, as revealed by trace element abundances. Journal of Geology,
732 88: 211-224.

733 McCarthy, T.S., Hasty, R.A., 1976. Trace element distribution patterns and their
734 relationship to the crystallization of granitic melts. Geochimica et
735 Cosmochimica Acta, 40(11): 1351-1358.

736 Naldrett, A.J., 1989. Magmatic Sulfide Deposits. Oxford University Press.

737 Nardi, L.V.S. et al., 2013. Zircon/rock partition coefficients of REEs, Y, Th, U,
738 Nb, and Ta in granitic rocks: Uses for provenance and mineral
739 exploration purposes. Chemical Geology, 335: 1-7.

740 Ollila, J.T., 1981. A fluid inclusion and mineralogical study of tin deposits and
741 rocks associated with the Bushveld Complex at the Zaaiplaats Rooiberg
742 and Union tin mines in the central Transvaal, South Africa, Rand
743 Afrikaans University, Johannesburg, 257 pp.

744 Palme, H., Lodders, K., Jones, A., 2014. Solar System Abundances of the
745 Elements. Treatise on Geochemistry, 2nd edition: 15-36.

746 Pettke, T., Audétat, A., Schaltegger, U., Heinrich, C.A., 2005. Magmatic-to-
747 hydrothermal crystallization in the W–Sn mineralized Mole Granite
748 (NSW, Australia). Chemical Geology, 220(3-4): 191-213.

749 Pollard, P.J., Andrew, A.S., Taylor, R.G., 1991a. Fluid Inclusion and Stable
750 Isotope Evidence for Interaction between Granites and Magmatic
751 Hydrothermal Fluids during Formation of Disseminated and Pipe-Style
752 Mineralization at the ZaaiplaatsTin Mine. Economic Geology, 86(121-
753 141).

754 Pollard, P.J., Taylor, R.G., Tate, N.M., 1989. Textural evidence for quartz and
755 feldspar dissolution as a mechanism of formation for Maggs Pipe,
756 Zaaiplaats tin mine, South Africa. Mineralium Deposita, 24: 210-218.

757 Pollard, P.J., Taylor, R.G., Taylor, R.P., Groves, D.I., 1991b. Petrographic and
758 Geochemical Evolution of Pervasively Altered Bushveld Granites at the
759 Zaaiplaats Tin Mine. Economic Geology, 86: 1401-1433.

760 Robb, L.J., Freeman, L.A., Armstrong, R.A., 2000. Nature and longevity of
761 hydrothermal fluid flow and mineralization in granites of the Bushveld
762 Complex, South Africa. Transactions of the Royal Society of Edinburgh:
763 Earth Sciences, 91: 269-281.

764 Schmidt, C., Romer, R.L., Wohlgemuth-Ueberwasser, C.C., Appelt, O., 2020.
765 Partitioning of Sn and W between granitic melt and aqueous fluid. Ore
766 Geology Reviews, 117.

Shen, P., Hattori, K., Pan, H., Jackson, S., Seitmuratova, E., 2015. Oxidation Condition and Metal Fertility of Granitic Magmas: Zircon Trace-Element Data from Porphyry Cu Deposits in the Central Asian Orogenic Belt. Economic Geology, 110: 1861-1878.

Sillitoe, R.H., 2010. Porphyry copper systems. Economic Geology, 105: 3-41.

Sun, S.s., McDonough, W.F., 1989. Chemical and isotopic systematics of oceanic basalts: implications for mantle composition and processes. Geological Society, London, Special Publications, 42(1): 313-345.

Vonopartis, L., Nex, P., Kinnaird, J., Robb, L., 2020. Evaluating the Changes from Endogranitic Magmatic to Magmatic-Hydrothermal Mineralization: The Zaaiplaats Tin Granites, Bushveld Igneous Complex, South Africa. Minerals, 10(4).

Walraven, F., 1982. Textural, geochemical and genetical aspects of the granophyric rocks of the Bushveld Comple, University of the Witwatersrand,, Johannesburg, South Africa, 258 pp.

Walraven, F., Hattingh, E., 1993. Geochronology of the Nebo Granite, Bushveld Complex. South African Journal of Geology, 96: 31-41.

Watson, E.B., Wark, D.A., Thomas, J.B., 2006. Crystallization thermometers for zircon and rutile. Contributions to Mineralogy and Petrology, 151: 413-433.

Whitney, J.A., Naldrett, A.J., 1989. Ore deposition associated with magmas. Reviews in Economic Geology, 4. Society of Economic Geologists, 250 pp.

Wilkinson, J.J., 2013. Triggers for the formation of porphyry ore deposits in magmatic arcs. Nature Geoscience, 6(11): 917-925.

Williams-Jones, A., Heinrich, C., 2005. Vapor Transport of Metals and the Formation of Magmatic-Hydrothermal Ore Deposits. Economic Geology, 100: 1287-1312.

Wood, S.A., Samson, I.M., 2000. The Hydrothermal Geochemistry of Tungsten in Granitoid Environments: I. Relative Solubilities of Ferberite and Scheelite as a Function of T, P, pH, and mNaCl. Economic Geology, 95: 143-182.

Zeh, A., Ovtcharova, M., Wilson, A.H., Schaltegger, U., 2015. The Bushveld Complex was emplaced and cooled in less than one million years – results of zirconology, and geotectonic implications. Earth and Planetary Science Letters, 418.

Figure and Table Captions

Figure 1. **A:** Cross-section of the Zaaiplaats tin deposit, with the Bobbejaankop – which hosts the central mineralized zone - and Lease granite units. Also shown are indicative tourmaline-cassiterite-chlorite rich 'pipes' in black, and conceptual sampling section (red line). After Pollard et al. (1989); **B:** Schematic section of sample localities with respect to their location within the vertical cross section, plotted at mean zircon Sn/Gd ratios, with the mineralized samples showing elevated Sn/Gd; samples 46/x and 47/x are from drill core, and ZA1/9 is a sample of pipe. **C:** Outline map of the Bushveld Complex, showing the location of the Zaaiplaats tin field within the Lebowa Granite Suite. **D:** Image of the Bobbejaankop granite cut through by a cassiterite and tourmaline-rich "pipe" feature. This clearly shows the characteristic "reddening" alteration. Hammer is 28 cm long.

Figure 2. Zaaiplaats zircon data, annotated by type and sample number. Plotting metal contents (Sn, Cu, Mo, W, Sm, Ti, Y, and Nb) versus Gd, a measure of fractionation. The plots of Sn and Cu clearly show elevated contents of these metals in the mineralized samples, unlike for Mo and W. The coincident trends in Sm vs Gd, Y vs Gd and Nb vs Gd reflect variations that relate to magma fractionation.

Figure 3. A: Chondrite (CHUR)-normalized plot of the average REE zircon content per sample, using the CHUR values of Palme et al. (2014); **B:** Primitive-mantle normalized plot of the average trace element zircon content per sample, using the primitive mantle values of Sun and McDonough (1989).

Figure 4. A: Zaaiplaats whole rock data, plotting TEDI, the trace element differentiation index (defined as [(Ba x Sr)/Rb]), versus Nb; this shows a fractionation trend (grey arrow) of increasing fractionation with decreasing TEDI, from the more primitive Nebo through to the Bobbejaankop and Lease units. Also plotted are the whole-rock data for the two samples 46/8 (unmineralized) and 47/10 (mineralized), both taken from the Bobbejaankop granite. The dotted grey box highlights the ten Nebo samples used for

deriving a starting composition for Rayleigh Fractionation modelling. **B, C:** Plotting Nb and Gd versus Y for the whole-rock data and for calculated melts in equilibrium with zircon using appropriate partition coefficients, for samples 46/8 and 47/10.

Figure 5. Zaaiplaats zircon data, plotting **A:** Gd against Ca; **B:** Sn against Ca; **B:** Sn against Gd; **D:** Pr/Yb versus Sm/Gd. Annotated by sample as per Figure 2.

Figure 6. A. Plot of zircon Sm/Gd versus zircon Y. Error bars on Sm/Gd ratios are 7 %, taken from the calculated uncertainties on reference measurements. **B.** Plot of zircon Sn/Gd versus Y, with error bars on Sn/Gd ratios of 15 %, taken from the calculated uncertainties on reference measurements. The interpreted Zaaiplaats fractionation trend (blue) and mineralization trend (red) are highlighted. **C.** Plot of Sn vs Gd at a log scale highlighting the development of order-of-magnitude elevated high-Sn values during magma fractionation.

Figure 7. The development of a metal anomaly Sn/Sn* as seen in zircon Sn/Gd as a function of magma fractionation (zircon Y). Highlighted is the mineralization step, the point at which excess Sn is added to the system, as a function of fluid:rock ratio and additional Sn, and which we calculate to occur at ~86 % crystallization of the host magma. After the mineralization step, fractionation continues. The red lines are fractionation trends of the upper and lower Sn/Gd values.

Table 1: Summary of samples taken from drill core Nos. 46 and 47, and surface sample ZA1, with approximate whole-rock Sn content.

Table 2: Modelling zircon Sn/Gd after the addition of excess Sn via a mineralizing fluid at F=0.14, as a function of fluid:rock ratio and ppm Sn. Highlighted in green are the Sn/Gd ratios that fall between the upper and lower boundaries (zircon Sn/Gd = 0.05 and 0.35) on Figure 7.

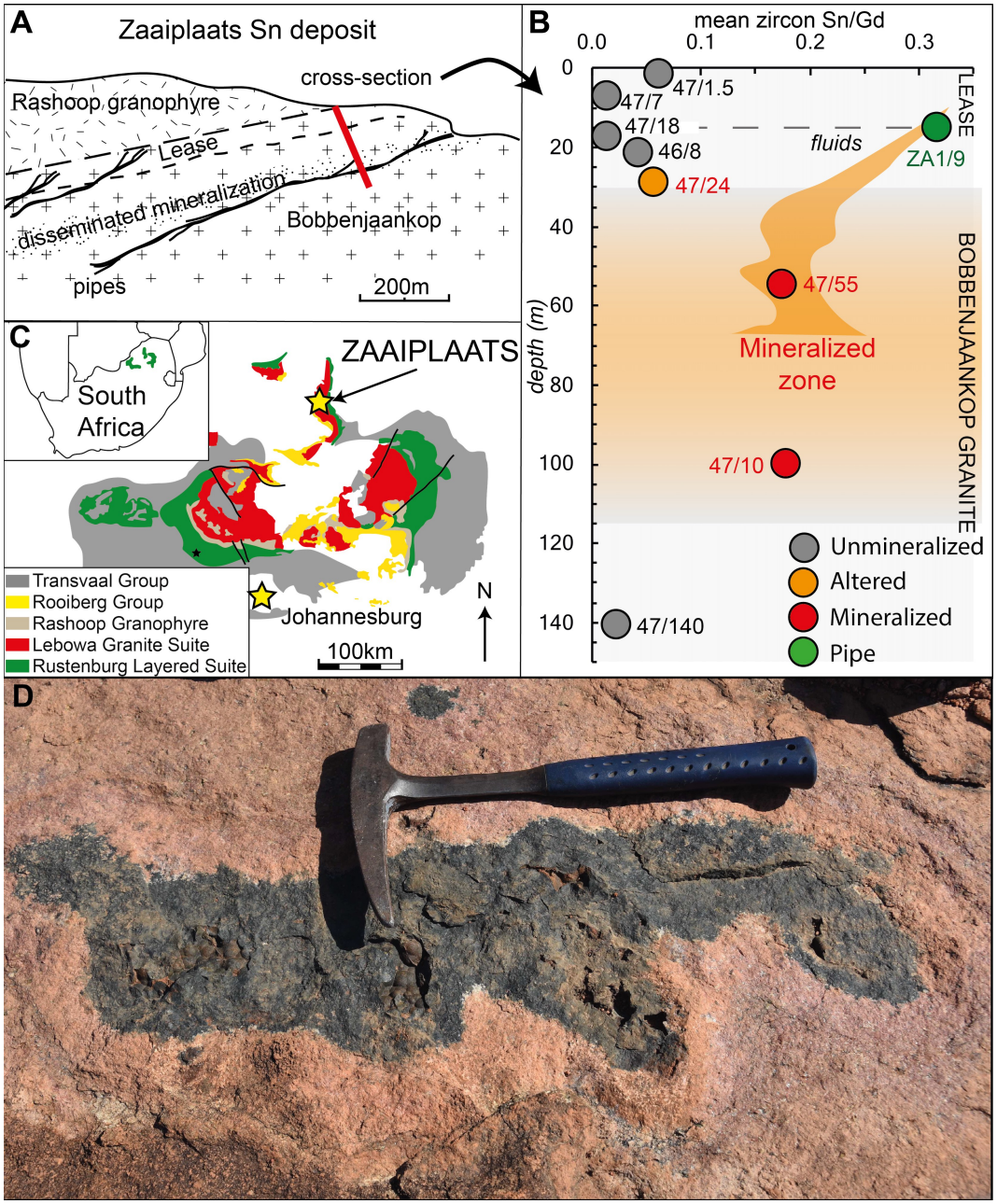

Fig 2

Click here to access/download;Figure;Figure2.pdf

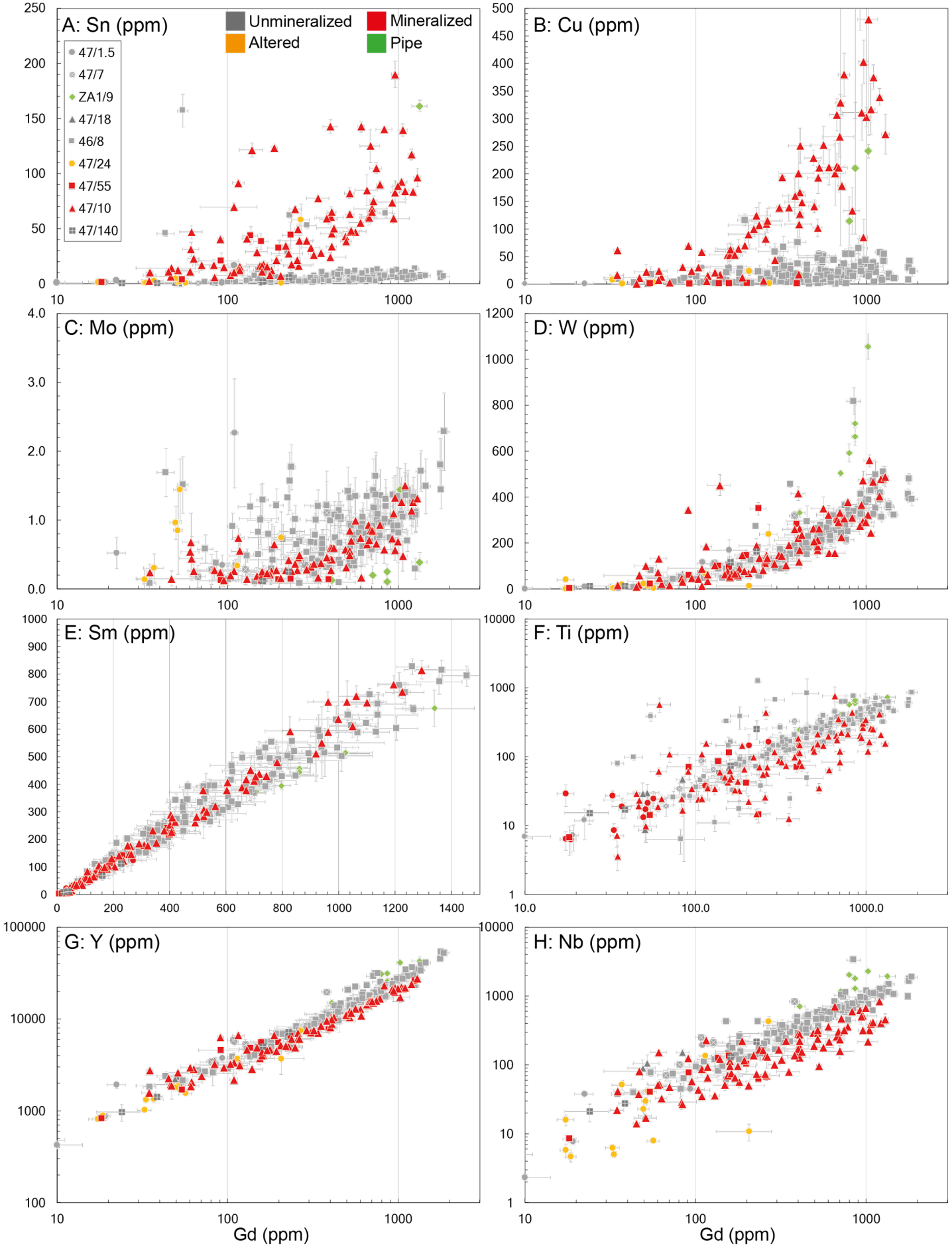

Fig 3

Click here to access/download;Figure;Figure3.pdf

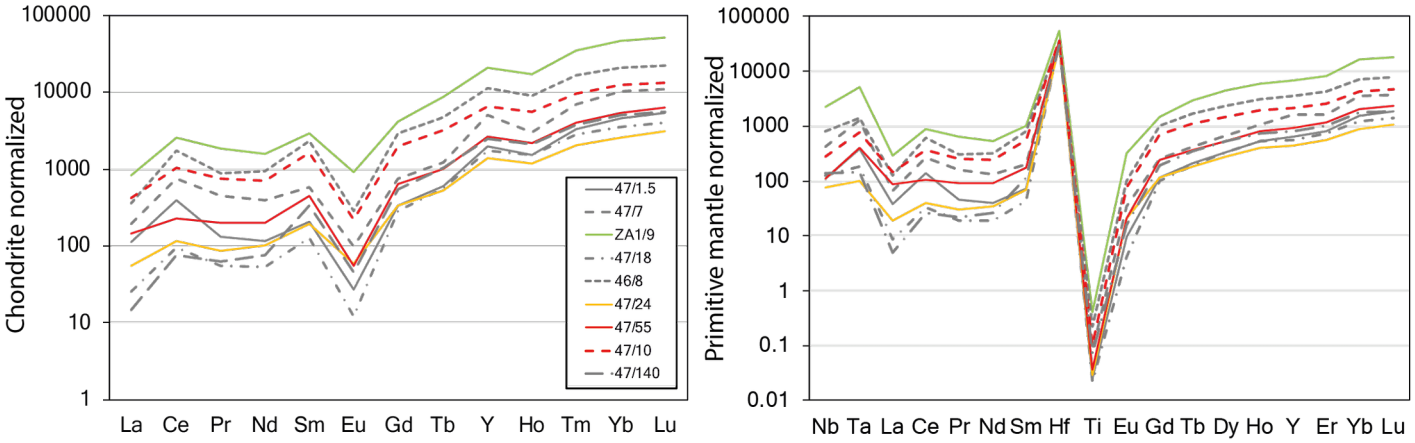

Fig 4

Click here to access/download;Figure;Figure4.pdf

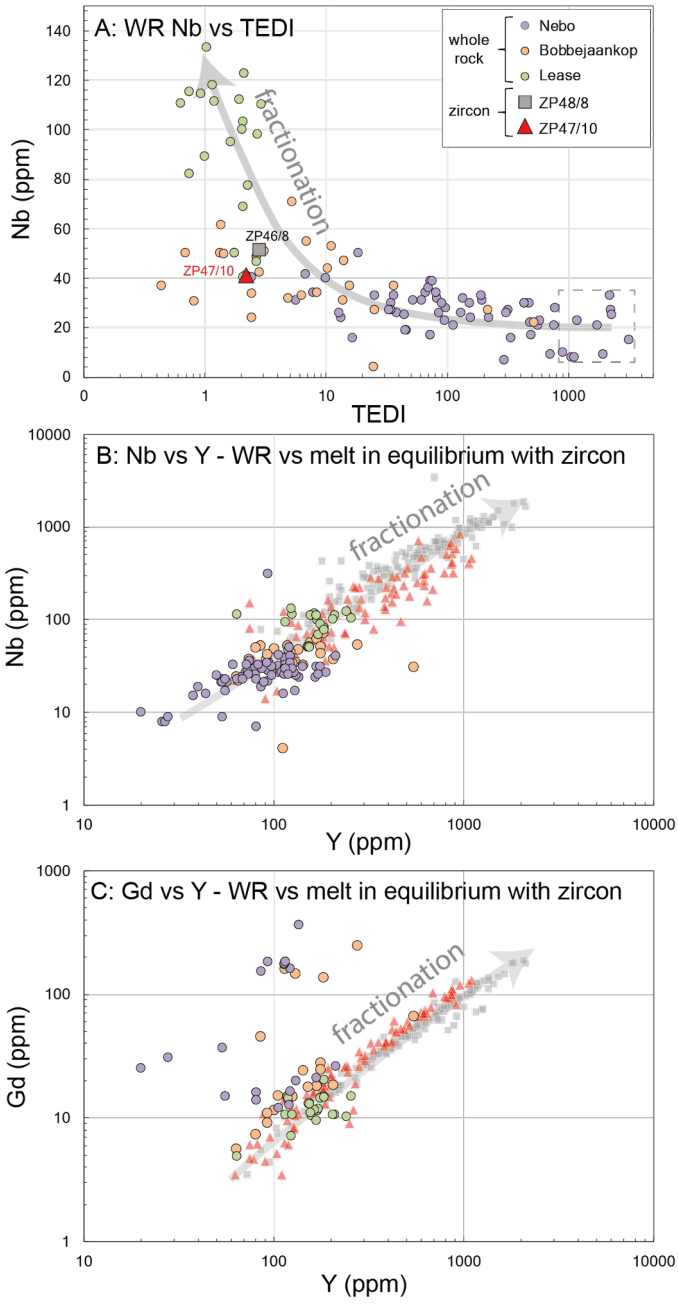

Fig 5

Click here to access/download;Figure;Figure5.pdf

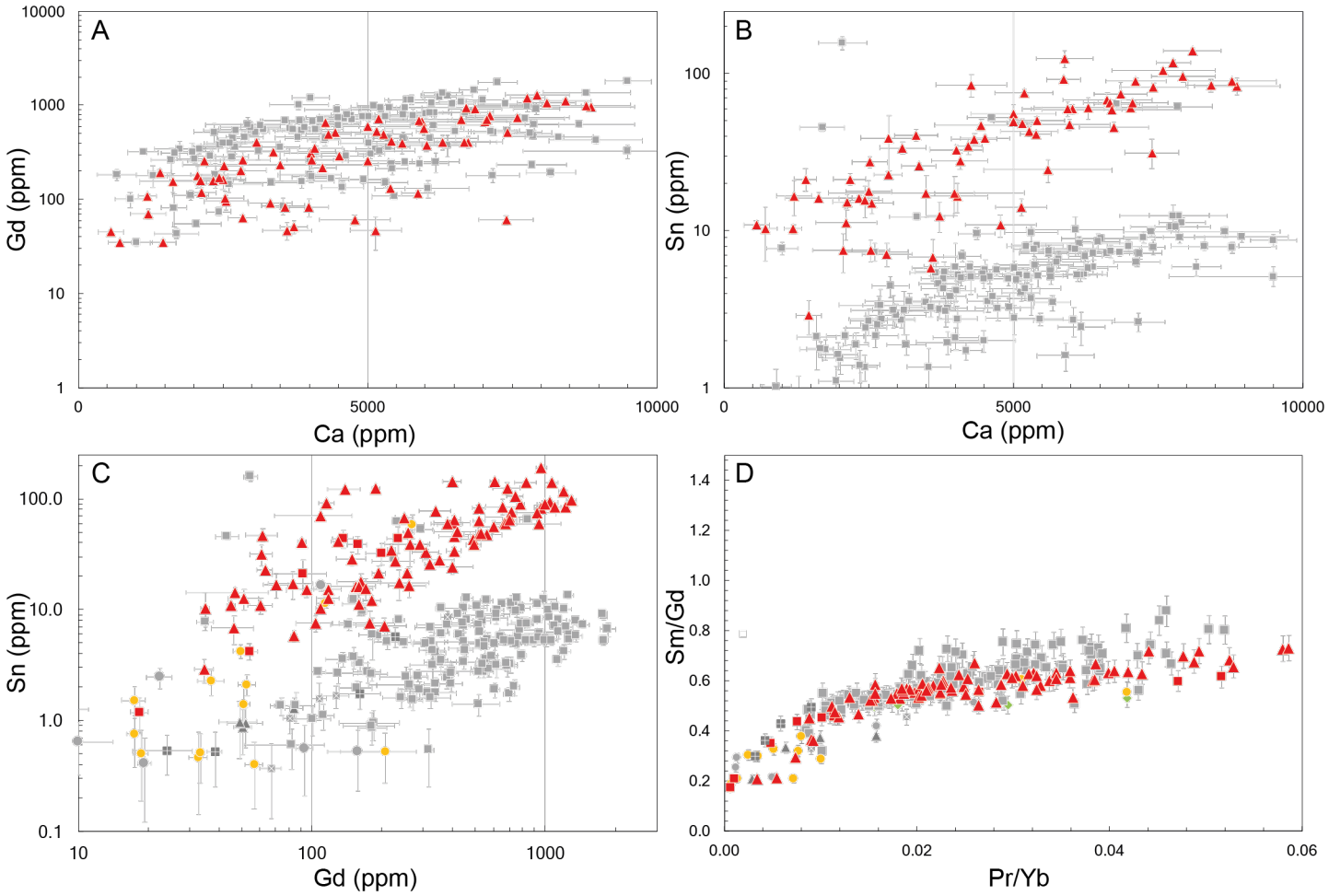

Fig 6

Click here to access/download;Figure;Figure6.pdf

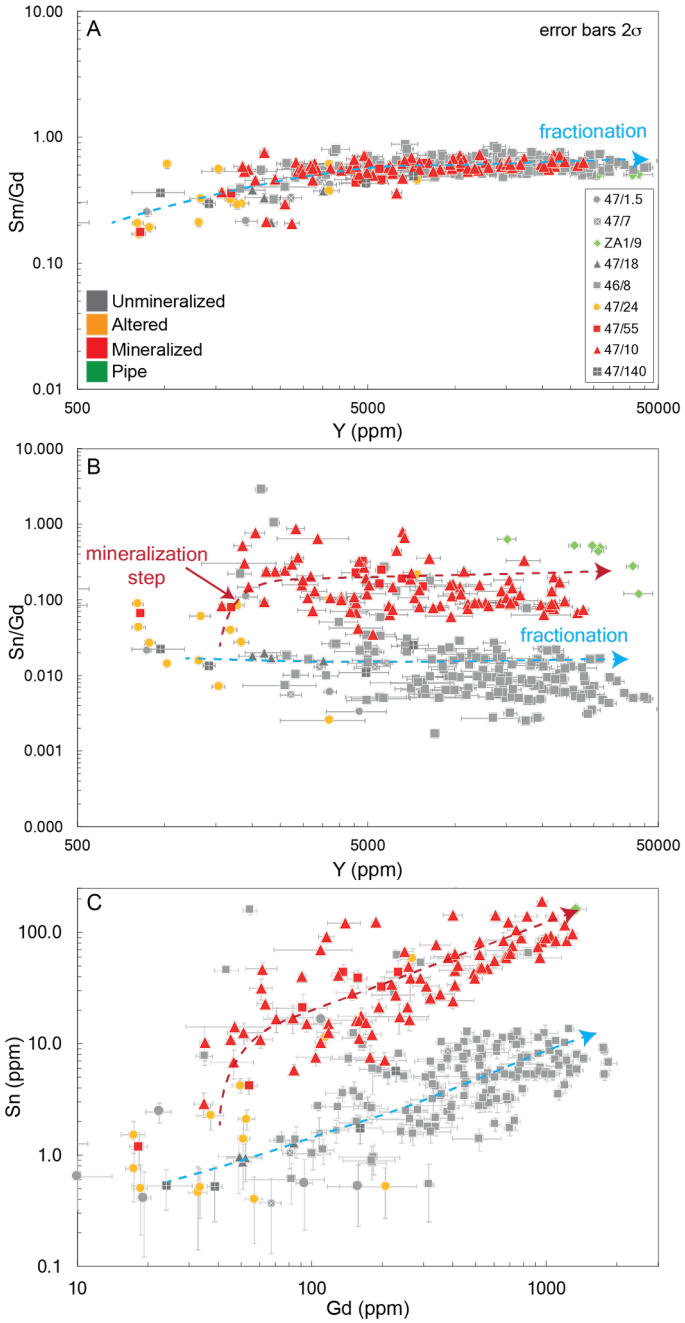

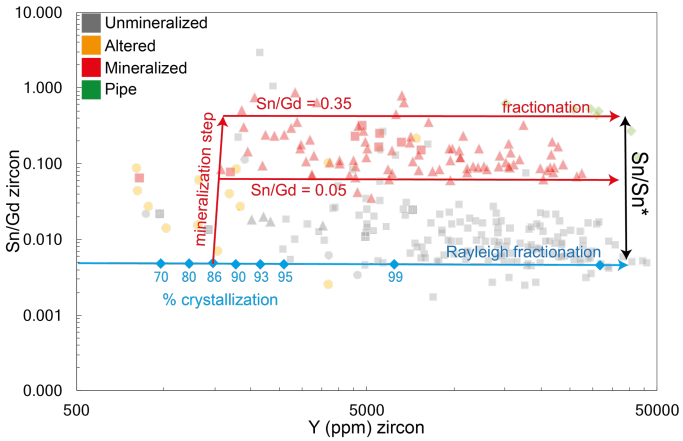

Sample	Unit		WR Sn ppm	Comments
47/1.5	Lease		<10	Unmineralized
47/7			<10	Unmineralized
ZA1/9				Mineralized pipe
47/18	Bobbejaankop	Upper	<10	Unmineralized
46/8		Upper	<10	Unmineralized
47/24		Upper	<10	Altered
47/55		Mineralized zone	562	Mineralized
47/10		Mineralized zone	354	Mineralized
47/140		Lower	<10	Unmineralized

Table 1: Summary of samples taken from drillcore Nos. 46 and 47, and surface sample ZA1, with approximate whole-rock Sn content.

Table 2: Modelling zircon Sn/Gd after the addition of excess Sn via a mineralizing fluid at F=0.14, as a function of fluid:rock ratio and ppm Sn. Highlighted in green are the Sn/Gd ratios that fall between the upper and lower boundaries (zircon Sn/Gd = 0.05 and 0.35) on Figure 7.

Fluid: Rock	Sn (ppm) 10	25	50	100	250	500	1000	2000	5000
0.01	0.00	0.01	0.01	0.01	0.01	0.02	0.03	0.05	0.12
0.02	0.01	0.01	0.01	0.01	0.02	0.03	0.05	0.10	0.24
0.03	0.01	0.01	0.01	0.01	0.02	0.04	0.08	0.15	0.36
0.05	0.01	0.01	0.01	0.02	0.03	0.06	0.12	0.24	0.60
0.1	0.01	0.01	0.02	0.03	0.06	0.12	0.24	0.48	1.19
0.15	0.01	0.01	0.02	0.04	0.09	0.18	0.36	0.71	1.78
0.2	0.01	0.02	0.03	0.05	0.12	0.24	0.48	0.95	2.37
0.25	0.01	0.02	0.03	0.06	0.15	0.30	0.60	1.19	2.96